

# Dual-stage servo systems and vibration compensation in computer hard disk drives<sup>☆, ☆ ☆</sup>

Roberto Horowitz<sup>a,\*</sup>, Yunfeng Li<sup>b</sup>, Kenn Oldham<sup>a</sup>, Stanley Kon<sup>a</sup>, Xinghui Huang<sup>c</sup>

<sup>a</sup>Computer Mechanics Laboratory (CML), Department of Mechanical Engineering, University of California at Berkeley, CA 94720-1740, USA

<sup>b</sup>Samsung Information Systems America, 75 West Plumeria Drive, San Jose, CA 95134, USA

<sup>c</sup>Servo Dynamics Group, Seagate Research, 1251 Waterfront Place, Pittsburgh, PA 15222, USA

Received 18 March 2005; received in revised form 26 July 2006; accepted 7 September 2006

## Abstract

This paper discusses two mechatronic innovations in magnetic hard disk drive servo systems, which may have to be deployed in the near future, in order to sustain the continuing 60% annual increase in storage density of these devices. The first is the use of high bandwidth dual-stage actuator servo systems to improve the precision and track-following capability of the read/write head positioning control system. The second is the instrumentation of disk drive suspensions with vibration sensing strain gages, in order to enhance airflow-induced suspension vibration suppression in hard disk drives.

© 2006 Published by Elsevier Ltd.

*Keywords:* Hard disk drives; Dual-stage servos; Vibration suppression; Instrumented suspensions

## 1. Introduction

Since the first hard disk drive (HDD) was invented in the 1950s by IBM, disk drives' storage density has been following Moore's law, doubling roughly every 18 months. Current storage density is 10 million times larger than that of the first HDD (Yamaguchi, 2001).

A current goal of the magnetic disk drive industry is to break the 1 Terra-bit per square inch storage density barrier. It is predicted that the necessary track density for 1 Terra-bit per square inch recording will be 500,000 tracks-per-inch (TPI), which requires a track mis-registration (TMR) budget of less than 5 nm (3-sigma value). To achieve such high track densities a new class of dual-stage actuation for HDDs has been proposed: a microactuator (MA) is placed at the end of the voice coil motor (VCM) suspension and moves the magnetic head (or slider) relative to the suspension, allowing increased servo bandwidth.

However, it has been determined through experimental tests, that slider motion due to airflow-induced suspension vibration is significant and becoming more important as the rotation speed of the drives increases. Since the major energy component of this motion is located at a frequency range that is higher than the expected servo bandwidth of even dual-stage servo systems, it cannot be compensated by the servo loop and, in fact, it may be amplified. This finding has been supported by the industry's own testing. As a consequence, suspension vibration compensation control schemes using instrumented suspensions and dual-stage servo systems are currently being investigated to overcome this problem. This paper presents an overview of some of these research activities.

Section 2 presents an overview of dual-stage servo systems in HDDs and discusses two different secondary actuation mechanism and configurations: PZT-actuated suspensions and MEMS MAs for actuating the slider. Section 3 focuses on the design and experimental implementation of dual-stage track-following servo systems using PZT-actuated suspensions. Section 4 discusses suspension vibration compensation using instrumented suspensions and dual-stage servo systems, focusing on active damping feedback control, where the signal from

<sup>☆</sup>Supported by the Information Storage Industry Consortium and the Computer Mechanics Laboratory of U.C. Berkeley.

<sup>☆☆</sup>Paper first presented as a plenary talk at the 3rd IFAC Symposium on Mechatronic Systems, September 6–8, 2004, Sydney, Australia.

\*Corresponding author. Tel.: +1510624675; fax: +15106435599.

E-mail address: [horowitz@me.berkeley.edu](mailto:horowitz@me.berkeley.edu) (R. Horowitz).

a strain sensor in an instrumented suspension is fed back in a minor loop configuration, to actively damp the VCM butterfly mode and the first suspension sway mode. The efficacy of this scheme is demonstrated using a dual-stage servo system that utilizes a PZT-actuated suspension. Section 5 discusses the determination of the optimal sensor location in an instrumented suspension, as well as the fabrication and micro-assembly of strain sensors in a steel suspension. Concluding remarks are presented in Section 6.

## 2. Dual-stage servo systems

The mechanical components of the servo system in a HDD include the VCM, the E-block, the suspension and the slider, as shown in Fig. 1(a). The magnetic read/write head is fabricated on the edge of the slider. The slider is supported by the suspension and flies over the surface of disk on an air-bearing. The VCM actuates the suspension with the slider about a pivot in the center of the E-block.

The two main tasks of a disk drive servo system are to move the head to the desired track as quickly as possible and, once on-track, position the head on the center of the track as precisely as possible so that data can be read/written quickly and reliably. The first task is commonly referred to as track seeking, while the second is commonly referred to as track following. The most commonly used performance measure for track-following servo systems is TMR, which is the variance of the deviation between the center of the read/write head and the center of the track. It is generally accepted in the magnetic recording industry that the  $3\sigma$  value of the TMR should be less than 10% of the track pitch. The deviation between the center of the

read/write head and the center of the track is in turn referred to as the head position error. The implementation of track-following servo systems relies on measuring the head position error signal (PES). The PES is generally obtained from information that is encoded on the magnetic disk, in angular servo sectors that radiate out from the center of the disk (Jorgenson, 1995). Since the servo sectors are located at discrete locations, the PES is a sampled digital signal and the disk drive control system is a digital control system. The sampling frequency is determined by the disk rotation speed and the number of servo sectors on a track. For example, a 7200-RPM disk drive with 180 servo sectors has a PES sampling frequency of 21.6 kHz. Given the disk rotation speed, higher PES sampling frequency requires more servo sectors and reduces storage efficiency.

Major TMR sources in the track-following mode include spindle runout, disk fluttering, bias forces including actuator pivot friction, external vibration/shock disturbances, arm and suspension vibrations due to air turbulence, PES noise, written-in repeatable runout and residual actuator and suspension vibration due to seek/settling (Ehrlich & Curran, 1999).

As data densities in HDDs increase and track widths diminish, single-stage, conventional servo systems become less able to successfully position the head. Because the voice coil/E-block/suspension assembly is large and massive as a unit, the speed at which the head can be controlled is limited. Furthermore, the assembly tends to have a low natural frequency, which can accentuate vibration in the disk drive and cause off-track errors. At track densities approaching one Terabit per square inch in the future, the vibration induced by airflow in a disk drive alone is enough to force the head off-track. Nonlinear friction of the pivot bearing also limits achievable servo precision. A solution to these problems is to complement the VCM with a smaller, second actuator to form a dual-stage servo system. The VCM continues to provide rough positioning, while the second actuator does fine positioning and rejects vibration and other disturbances. The smaller second actuator can typically be designed to have a much higher natural frequency and less susceptibility to vibration than the VCM. Any actuator used in a dual-stage system should be inexpensive to build, require little power to operate, and preserve the suspension stiffness properties to maintain an appropriate slider flying height. A number of different secondary actuation mechanism and configurations have been proposed. These can be categorized into three groups: “actuated suspension”, “actuated slider” and “actuated head”. The first two approaches will now be discussed in some detail.

### 2.1. PZT-actuated suspensions

In this approach, the suspension is re-designed to accommodate an active component, typically a piezoelectric material such as PZT. This piezoelectric material

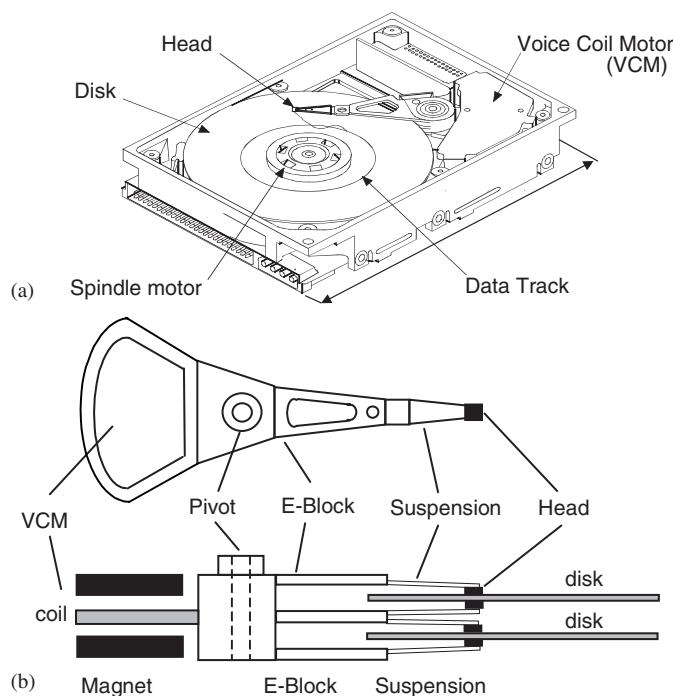


Fig. 1. (a) Conventional disk drive configuration; (b) conventional disk drive servo assembly.

stretches or flexes the suspension to position the slider and magnetic head. Piezoelectric actuators normally produce large actuation forces but small actuation strokes. Therefore, in the “actuated-suspension” configuration, piezoelectric actuation is usually complemented by a leverage mechanism that converts small actuator displacements into sufficiently large head displacements, as shown in Fig. 2(a).

An advantage of this approach is that the secondary-stage actuation can be implemented in a relatively simple manner, by modifying the suspension design, without requiring significant changes in the suspension fabrication process. Moreover, this dual-stage servo configuration is effective in attaining low-frequency runout attenuation in the servo loop. The major drawback of this approach is that the suspension design modifications that are necessary to implement the leverage mechanisms that convert small piezo-actuator displacements into sufficiently large head displacements, weaken some of the suspension off-track resonance modes, such as the first sway and torsional modes. These modes limit the attainable track-following servo bandwidth and are in turn excited by airflow. Thus, track-per-inch (TPI) servo performance using piezo-actuated suspensions can be increased, but remains limited when compared to the next two approaches (Chen, 2001; Evans, Griesbach, & Messner, 1999; Koganezawa, Takaishi, Mizoshita, Uematsu, & Yamada, 1997; Kuwajima & Matsuoka, 2002; Naniwa, Nakamura, Saegusa, & Sato, 1999).

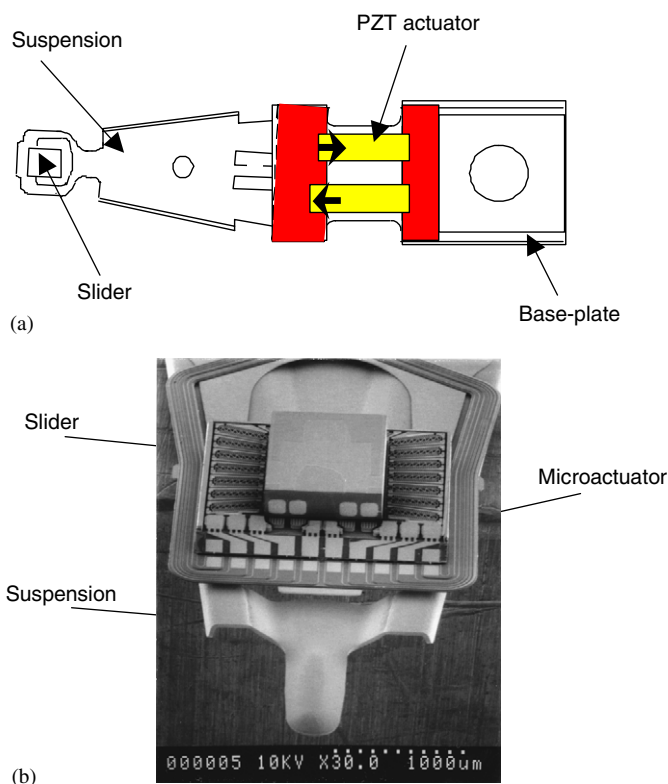


Fig. 2. (a) PZT-actuated suspension (Courtesy of M. Kobayashi, Hitachi); (b) electrostatic rotational MEMS microactuator (Courtesy of L.-S. Fan, IBM).

### 2.1.1. Frequency response of a PZT-actuated suspension

The PZT-actuated suspension described in this section was provided by Hutchinson Technologies and has a stroke limit of  $\pm 1 \mu\text{m}$  under a driving voltage of  $\pm 40 \text{ V}$ . It was installed on the top finger of the E-block in a 7200-RPM disk drive. Head lateral motion was detected by an LDV. An opening was cut on the side of the disk drive to allow the LDV's laser to pass through. The PZT-actuated suspension was modified so that only one of its PZT elements was used as a second-stage actuator, while the other was used as a strain sensor.

Fig. 3(a) shows the measured and simulated frequency responses of the PZT-actuated suspension. The solid lines are experimentally measured responses, while the dashed lines are simulated responses using an identified model. As shown in these figures, the major vibration modes of the PZT-actuated suspension dual-stage actuator in this setup include the assembly butterfly mode (M1 in the figures), the suspension sway mode (M2), the suspension second torsion mode (M3), and the suspension 1st torsion mode (M4). Among them, the two most important off-track modes are the E- butterfly mode and the suspension sway mode. The assembly butterfly mode is generated by the coupling of in-plane sway modes of the E-block arm and the coil, in which the arm and the coil move out of phase with respect to each other around the pivot. The suspensions sway mode is the mode in which the load beam and the slider vibrate with respect to the hinge of the PZT-actuated suspension. It is also called the PZT actuator mode. The torsion modes of the suspension also contribute to head off-track motion. The frequency response from VCM input  $u_1$  to head displacement  $y_1$  is dominated by the rigid body mode in the low-frequency range and the structural vibration modes in the high-frequency range. Fig. 3(b) shows that the PZT actuator can excite the VCM actuator butterfly mode through the swage connection with the E-block arm.

### 2.2. Actuated slider

In this approach, a MA is placed between the slider and the gimbal, to create either a translational or rotational in-plane rigid body motion of the slider relative to the suspension tip, which acts as a fine-positioning mechanism for the read/write head, as shown in Fig. 2(b). The resulting bandwidth of dual-stage servo systems that utilize the actuated slider approach can be higher than those that utilize the piezo-actuated suspension approach because the secondary actuation mechanism in the actuated slider approach bypasses the mechanical resonances of the suspension. This approach uses existing sliders and MAs that can be batch fabricated, and thus could be cost effective. However, the size and mass of the MA may affect the slider flying stability. Therefore, current suspensions need to be re-designed to adopt this secondary actuator. Suitable driving forces in this approach include electrostatic, electromagnetic and piezoelectric (Fan et al., 1999; Horsley, 1998; Koganezawa et al., 1997). To further reduce

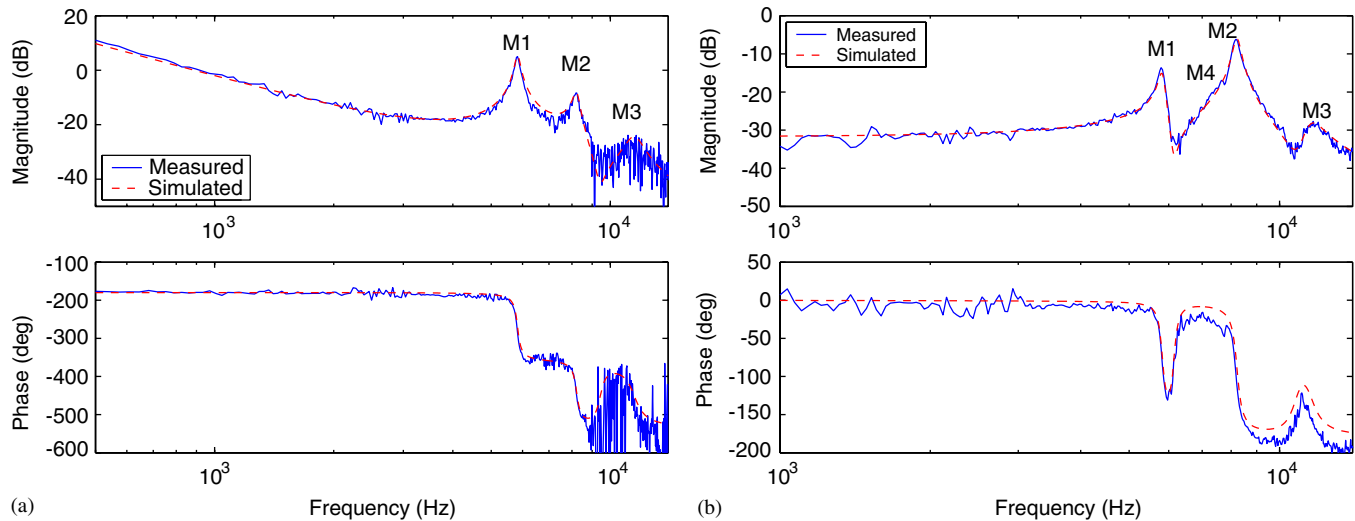


Fig. 3. PZT-actuated suspension frequency response: (a) from VCM input to head displacement; (b) from PZT actuator input to head displacement.

the assembly task of placing the MA in between gimbal structure and slider, some researchers have proposed MAs that are either integrated with the gimbal structure (Muller, 2000) or the slider (Imamura et al., 1998).

### 3. Dual-stage track-following servo design techniques

As described in Section 2, the primary objective of the track-following servo system is to minimize head TMR, which is the variance of the deviation between the center of the read/write head and the center of the track, in the presence of stochastic (non-repetitive) and deterministic (repetitive) disturbances and actuator unmodelled dynamics and parametric uncertainties. For dual-stage servos, two additional constraints must be considered. The first one is that the contribution of each actuator to the closed-loop sensitivity transfer function attenuation must be properly allocated in the frequency domain. In general, the first-stage coarse motion actuator has a large moving range, but its bandwidth is limited by the existence of poorly damped off-track E-block and suspension resonance modes. Thus, its contribution to the sensitivity transfer function attenuation must be primarily in the low-frequency range. On the other hand, the second-stage fine motion actuator can operate at a higher-frequency range but has a significantly smaller range of motion. Thus, its contribution to the sensitivity transfer function attenuation must be primarily in the high-frequency range. The second constraint is that, any destructive effect, in which two actuators move in opposite directions producing little overall net head compensation motion, should be avoided (Schroeck, Messner, & McNab, 2001).

Various control design architectures and methodologies have been developed for dual-stage servo control design. They can be largely classified into two categories: those based on classical SISO design methodologies, and those based on modern optimal and robust design methodolo-

gies. Most of the proposed classical SISO design methodologies perform some form of decoupling control, followed by sequential multiple SISO compensator loop shaping designs, in order to shape the overall closed-loop sensitivity transfer function frequency response. Examples of these techniques include the master-slave and decoupled sensitivity design approaches (Li & Horowitz, 2001; Mori, Munemoto, Otsuki, Yamaguchi, & Akagi, 1991; Suthasun, Mareels, & Al-Mamun, 2004), the PQ design method (Schroeck et al., 2001), and a direct parallel design approach (Semba, Hirano, & Fan, 1999). Since dual-stage servos are multi-input systems, it is natural to utilize modern state-based optimal and robust MIMO methodologies to design dual-stage track-following controllers. Dual-stage control designs using LQG and LQG/LTR have been reported in Suzuki et al. (1997), Hu, Guo, Huang, and Chen (1999), Suh, Chung, and Lee (2002) and others. Robust MIMO designs based on  $H_\infty$  and  $\mu$ -synthesis design methodologies have been reported in Suzuki et al. (1997), Hernandez, Park, Horowitz, and Packard (1999), Rotunno and de Callafon (2000), Li and Horowitz (2002), Herrmann and Guo (2004) and others. The design of multi-rate and multi-sensing dual-stage track-following servos using mixed objective optimization techniques have been recently presented in Huang, Nagamune, Horowitz, and Li (2004), Huang and Horowitz (2005), where the  $H_2$  norm of the closed-loop sensitivity transfer function is minimized, while simultaneously attaining  $H_\infty$  norm bounds on the VCM and MA complementary sensitivity transfer functions, and in Nagamune, Huang, and Horowitz (2005), de Callafon, Nagamune, and Horowitz (2006), Huang, Nagamune, and Horowitz (2006), where the design of robust  $H_2$  track-following controllers for dual-stage servo systems is presented. In the remainder of this section, the decoupled sensitivity design approach to the design of track-following servos that utilize the PZT-actuated suspension described



in Section 2.1 will be briefly reviewed. Further details of the results presented in this section, as well as other design techniques, can be found in (Li, 2003).

3.1. Track-following SISO design specifications

Traditional robustness and performance specifications for a typical track-following servo design are specified in terms of its open-loop gain and phase margins, its bandwidth and its closed-loop sensitivity maximum peaking. For the feedback system to be robust, a gain margin larger than 6 dB and a phase margin larger than 35° is usually specified. Bandwidth is often characterized by the system’s open-loop gain crossover frequency. For single-stage actuator servo systems, the achievable bandwidth is limited by high-frequency resonance modes to within 1 kHz. Dual-stage actuator servo systems can achieve more than 2 kHz bandwidth. A closed-loop sensitivity maximum peak of 6 dB is usually specified, to minimize high-frequency disturbance/noise amplification beyond the servo bandwidth.

3.2. Sensitivity decoupling design

Fig. 4 shows a block diagram of the dual-stage controller design using sensitivity decoupling method. For simplicity, the PZT-actuated suspension will be referred to as the MA in this paper, while the VCM, E-block and suspension assembly will be referred to as the VCM. In Fig. 4,  $G_{VCM}(z)$  and  $G_{MA}(z)$  represent the VCM and MA models, respectively.  $K_{VCM}(z)$  and  $K_{MA}(z)$  represent the VCM and MA-loop controllers, respectively.  $r$  denotes the track runout.  $z$  denotes the absolute position of the head, while  $z_{VCM}$  denotes the position of the suspension tip, if it was not actuated by the PZT actuator. For simplicity,  $z_{VCM}$  will often be referred to as the position of the VCM.  $PES$  denotes the position error between the head and the center of the track, while  $RPES = z - z_{VCM}$  denotes the position of the head (MA) relative to the unactuated suspension tip.  $u_{VCM}$  and  $u_{MA}$ , respectively, denote the VCM and MA control inputs. The sensitivity decoupling control approach combines the  $PES$  and the  $RPES$  signals to generate the position error of the suspension tip relative to the track, which will be denoted by  $VPES$ ,

$$VPES = PES + RPES = r - z_{VCM}, \tag{1}$$

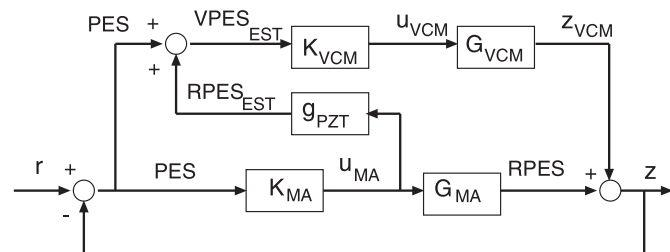


Fig. 4. Block diagram of the track-following controller design using the sensitivity decoupling method.

and this signal is fed to the VCM-loop compensator to decouple the control system (Mori et al., 1991).

Assuming that the relative position error signal,  $RPES$ , is available (i.e.  $RPES_{EST} = RPES$ ), the closed-loop sensitivity transfer function  $S_T(z)$  (from  $r$  to  $PES$ ) of the feedback system in Fig. 4 is given by

$$S_T(z) = \frac{1}{\underbrace{1 + K_{VCM}(z)G_{VCM}(z)}_{S_{VCM}(z)}} \frac{1}{\underbrace{1 + K_{MA}(z)G_{MA}(z)}_{S_{MA}(z)}} \tag{2}$$

and the block diagram in Fig. 4 is equivalent to the block diagram shown in Fig. 5. Thus, the dual-stage servo control design can be decoupled into two independent SISO sensitivity function shaping designs: the VCM loop, in which the runout  $r$  is first attenuated by the VCM-loop sensitivity function,  $S_{VCM}(z)$ , to produce  $VPES$ ; and the MA loop, in which this signal is further attenuated by  $S_{MA}(z)$  to produce the  $PES$ .

For most PZT-actuated suspensions, the relative position signal,  $RPES$ , is not available. An estimate of it,  $RPES_{EST}$ , can be obtained by multiplying the PZT control input by the DC gain of the PZT actuator,  $g_{PZT}$ . This estimate is accurate in the low-frequency range since the dynamics of the PZT actuator can be accurately characterized by a pure gain up to about 4 kHz, as shown in Fig. 3(b). Above this frequency, its dynamics are dominated by the E-block and suspension resonance modes. The estimation of  $RPES$ , using a constant gain, introduces an additional term in the open-loop transfer function of the actual feedback block in Fig. 4. However, generally both compensators  $K_{MA}(z)$  and  $K_{VCM}(z)$  are designed to have notch filters at the resonance frequencies, where the model error is large. Furthermore, the VCM loop gain crossover frequency is generally designed to be far lower than the E-block and suspensions resonance frequencies. As a consequence, the effect of this additional error term in the overall sensitivity transfer function  $S(z)$  is generally small.

3.2.1. A design example

A track-following compensator for a dual-stage servo system with a PZT-actuated suspension described in Section 2.1 was designed using the sensitivity decoupling technique and tested.

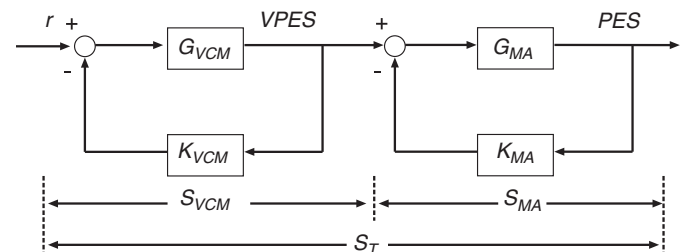


Fig. 5. Equivalent sensitivity function block diagram.

The VCM compensator,  $K_{VCM}(z)$ , was designed to be a simple lead-lag compensator cascaded with two notch filters. The lag compensator increases the control gain and error rejection in the low-frequency region, while the lead compensator boosts the phase margin at the open-loop gain crossover frequency. The notch filters were used to attenuate the butterfly mode (5.9 kHz) and the suspension sway mode (8.4 kHz), respectively. The VCM transfer function,  $G_{VCM}(z)K_{VCM}(z)$ , was calculated to have a gain crossover frequency of 800 Hz. The sampling frequency of the control system is 25 kHz. The dashed lines in Figs. 6, and 7(a) show the Bode plots of the VCM transfer function  $G_{VCM}(z)K_{VCM}(z)$ , and the closed-loop sensitivity function,  $S_{VCM}(z)$ , in Eq. (2), respectively.

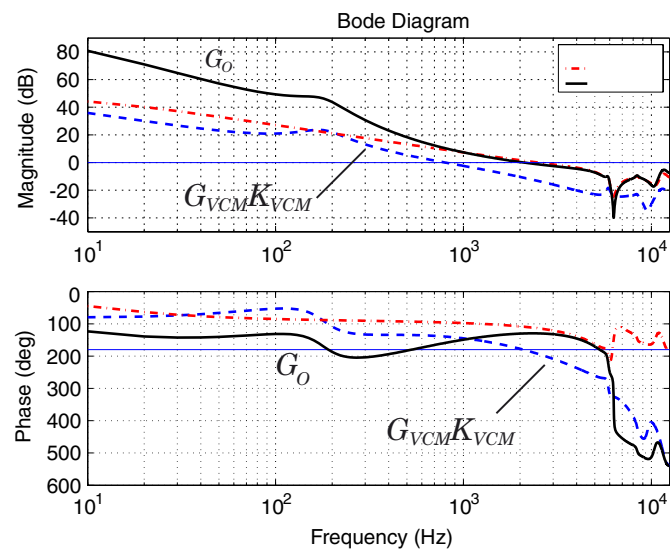
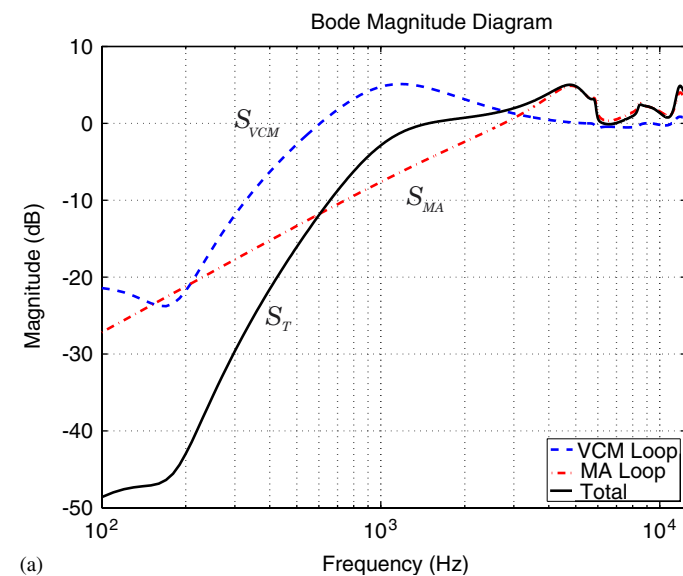


Fig. 6. Bode plots of  $G_{VCM}(z)K_{VCM}(z)$ ,  $G_{MA}(z)K_{MA}(z)$ , and the overall open-loop transfer function  $G_o(z)$  in Eq. (3).



(a)

The PZT actuator compensator,  $K_{MA}(z)$ , was designed to be a lag compensator cascaded with two notch filters that were similar to the ones designed for the VCM loop. Since the frequency response of the PZT actuator is almost flat in the low-frequency range, a lag compensator was used to provide the control gain for error rejection. The gain crossover frequency of the PZT actuator loop was designed to be approximately 2500 Hz ( $\frac{1}{10}$  of the sampling frequency), which is much higher than that of the VCM loop. The dotted lines in Figs. 6 and 7(a) show the Bode plots of the PZT actuator transfer function,  $G_{MA}(z)K_{MA}(z)$ , and the closed-loop sensitivity function,  $S_{MA}(z)$ , in Eq. (2), respectively.

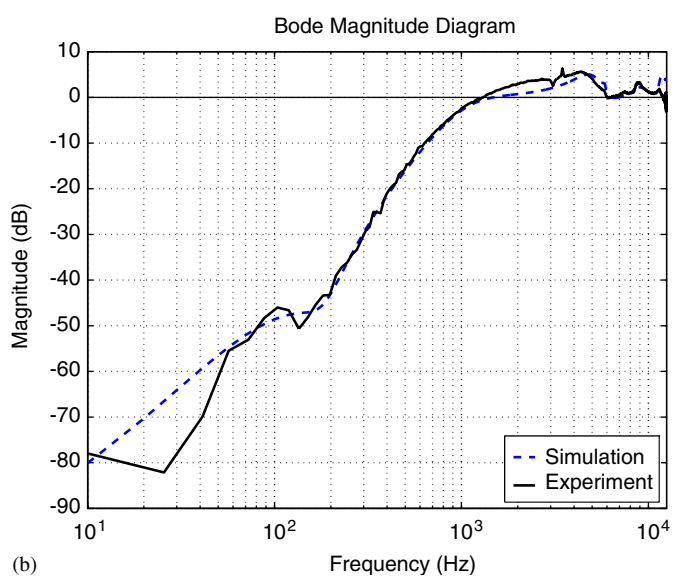
The VCM and PZT actuator-loop compensators designed above were used in the block diagram of the dual-stage control system depicted in Fig. 4. The solid lines in Figs. 6 and 7(a) show the Bode plots of the overall open-loop transfer function from the center of the track,  $r$ , to the head position,  $z$ , which is given by

$$G_o(z) = [1 + g_{PZT}K_{MA}(z)]G_{VCM}(z)K_{VCM}(z) + G_{MA}(z)K_{MA}(z), \quad (3)$$

and the closed-loop sensitivity function,

$$S_T(z) = \frac{1}{1 + G_o(z)}, \quad (4)$$

respectively. Table 1 lists the gain margins, phase margins, and gain crossover frequencies of the VCM transfer function  $G_{VCM}(z)K_{VCM}(z)$ , the PZT actuator transfer function  $G_{MA}(z)K_{MA}(z)$ , and the overall open-loop transfer function,  $G_o(z)$  in Eq. (3). As can be seen from Fig. 6, the overall open-loop frequency response near its gain crossover frequency is dominated by that of the PZT actuator loop. A simple tuning process was conducted to satisfy the design specifications by changing the corner



(b)

Fig. 7. (a) Bode plots of simulated sensitivity transfer functions  $S_{VCM}(z)$ ,  $S_{MA}(z)$  and  $S_T(z)$ ; (b) Bode plots of the simulated (dashed) and experimentally measured sensitivity transfer function  $S_T(z)$ .

Table 1  
Sensitivity decoupling design results

	GM (dB)	PM (deg)	Gain c/o frequency (Hz)
$G_{MA}(z)K_{MA}(z)$	10.9	40.5	800
$K_{VCM}(z)G_{VCM}(z)$	9.7	66.1	2500
$G_o(z)$ in (3)	7.4	50.2	2104
Design specifications	6	35	2000

frequency of the zero of the PZT actuator loop lag compensator. Increasing this frequency improves the overall gain margin, but reduces the phase margin and increases sensitivity function peaking, and visa versa. It was determined in simulations that an optimal value of this corner frequency is 2500 Hz to satisfy all the gain margin, phase margin and sensitivity function peaking requirements.

Fig. 7(a) shows the Bode plots of the VCM sensitivity function  $S_{VCM}(z)$  in Eq. (2), the PZT actuator sensitivity function  $S_{MA}(z)$  in Eq. (2), and the actual total sensitivity function  $S_T(z)$  in Eq. (4). The unity-gain frequency of  $S_T(z)$  is 1490 Hz, and the maximum peaking is 5.0 dB occurring at 4760 Hz. Notice that, as expected, the actual total sensitivity function  $S_T(z)$  is approximately the product of the sensitivity functions of the VCM loop and PZT actuator loop. A large attenuation is obtained in the low-frequency region with both sensitivity functions attenuating the error. However, the total sensitivity function  $S_T(z)$  has less attenuation in the mid-frequency range, from about 700 Hz to about 2 kHz, than that of the PZT actuator sensitivity function  $S_{MA}(z)$ . This is due to the amplification by the VCM loop sensitivity function  $S_{VCM}(z)$  over its unity-gain frequency at about 700 Hz. Relatively poor mid-frequency error rejection performance is one drawback of the sensitivity decoupling design method.

The designed controller was implemented using the experimental setup described in Section 2.1.1. Fig. 7(b) shows the Bode plots of the measured and simulated total sensitivity function  $S_T(z)$ . In general, the experimental data agrees well with the simulation data. The actual sensitivity unity-gain frequency is 1321 Hz (vs. 1490 Hz in the simulation). The actual sensitivity function maximum peaking is 6.3 dB occurring at 3460 Hz (vs. 5 dB occurring at 4760 Hz in the simulation).

#### 4. Suppression of air flow-induced vibrations

Airflow generated by the spinning disk is necessary to sustain the slider air-bearing, which in turn maintains a proper head flying height above the disk. However, it also induces structural vibrations in the suspension and arm's E-block. As the servo system's TMR requirements approach the range of 5–10 nm, these airflow induced vibrations become a more significant source of the TMR

budget, which must be attenuated. However, most of the air flow excitable structural resonance modes are in a frequency range that is higher than the attainable actuator servo bandwidth, which is constrained by the rotational speed of the disk and the percentage of the disk that can be dedicated to store sector servo information. As a consequence, airflow-induced vibration is often amplified rather than attenuated by the servo system. The characterizations of airflow induced structural vibrations have been reported in Yamaguchi, Takahashi, Fujita, and Kuwahara (1986), Kim and Mote (1999); Gross (2003) and others. It has been found that the magnitude of the air flow induced vibration is proportional to the square of the flow speed (Yamaguchi et al., 1986), and the airflow affects head off-track motion mainly by exciting the actuator structural resonance modes (Gross, 2003; Kim & Mote, 1999).

One method of improving servo capabilities to overcome these problems is to instrument the suspension with strain sensors (Huang, Banther, Mathur, & Messner, 1999; Huang, Horowitz, & Li, 2005; Li, 2003; Li, Horowitz, & Evans, 2003; Li, Marcassa, Horowitz, Oboe, & Evans, 2003). Adding sensors to the suspension permits acquisition of vibration information at a higher sampling rate and closer to the point of disturbance than is possible from position error signals taken from the disk itself. This information may be fed back to the VCM or actuated suspension or fed forward to actuated sliders and heads. Micro-scale processing techniques allow precise installation of vibration sensors at locations with maximal vibration information. Moreover, certain semiconductor and thin film processing techniques produce very high sensitivity gages, and may potentially be integrated into suspension fabrication and assembly. Different control schemes for suspension vibration compensation are needed depending on the type and configuration of dual-stage actuators. The PZT actuators on PZT-actuated suspensions are located behind the suspension and can excite the suspension dynamics. In this case, feedback active damping control can be applied. The MEMS MA of an actuated-slider dual-stage servo system has little effect on the suspension dynamics. In this case, feedforward control can be used to cancel the TMR induced by the suspension vibration.

##### 4.1. Damping control of PZT-actuated suspensions

It is possible to use the same PZT elements that are used for actuation as strain sensors, in order to measure vibration in the suspension and the E-block, as discussed in Li, Horowitz, et al. (2003, Li, Marcassa, et al. (2003). Specifically, a PZT-actuated suspension such as the one depicted in Fig. 2, can be modified so that one of the two PZT elements in the suspension is used as vibration sensor, while the other is used as an actuator. This modification reduces the effective PZT-actuator gain by half. However, in most situations, the resulting PZT actuation gain is sufficient to achieve adequate track following. The vibration signal from the PZT element can be fed into a

minor-loop vibration damping controller to damp out some the major resonance modes that are excited by airflow. Fig. 8 shows the power spectral densities (PSD) of the head off-track position  $z$  (upper half), and the PZT sensor output  $y$  (lower half), when the spindle is rotating in a 7200-RPM disk drive, for the system described in Section 2.1.1. As shown in the figure, the major off-track modes excited by air flow turbulence generated by disk rotation include the butterfly mode (M1), the suspension sway mode (M2) as well as the 1st and 2nd torsion modes (M4 and M3).

Fig. 9 shows the measured and simulated frequency responses: from the VCM input  $u_{VCM}$  to PZT sensor output  $y$  and from the PZT actuator input  $u_{MA}$  to PZT sensor output  $y$ . The solid lines are experimentally measured responses, while the dashed lines are simulated

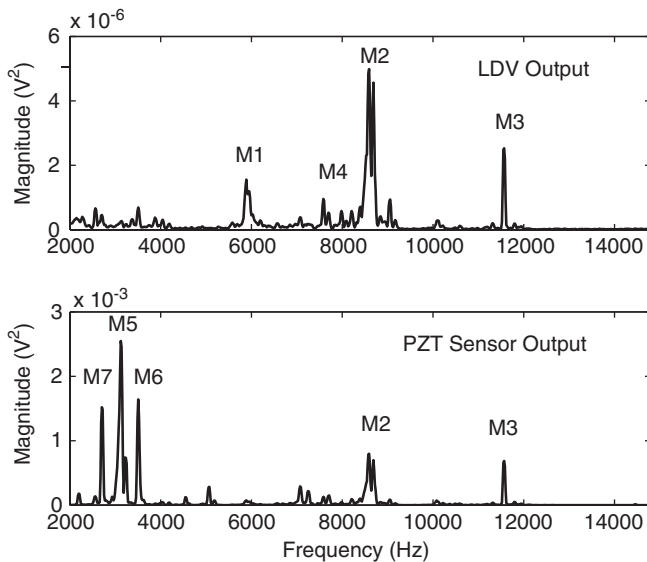


Fig. 8. PSDs of the head off-track position,  $z$  (top), and the PZT sensor output,  $y$  (bottom), due to airflow excited vibrations.

responses using an identified model. As shown in Figs. 8 and 9(b), the PZT sensor can pick up most of the off-track vibration modes of the head stack and suspension assembly when they are excited by air flow and the control inputs. The PZT sensor does not sense the rigid body mode, as expected. However, the PZT sensor picks up some non-off-track modes near 3 kHz (M5, M6, and M7), which have little effect on the head off-track motion. These modes are probably related to the bending modes of the suspension and they are excited by the air flow disturbances in the out-of-the-plane direction. They act as noise modes to the vibration suppression control system.

Fig. 10 shows the block diagram of a PZT-actuated dual-stage servo system with an inner-loop vibration damping control.  $P$  represents the augmented plant model, which will be described subsequently, and  $w$  represents the air flow disturbances acting on the system. The damping controller is implemented using the PZT sensor output  $y$ , so that its sampling frequency will not be limited by that of the  $PES$ .

As shown in Figs. 8 and 9(b), modes, modes M5, M6, and M7 have a large contribution to the PZT sensor output when excited by airflow disturbances, but have little contribution to the head off-track motion. Moreover, they are either not controllable or weakly controllable by the control inputs. Thus, they need to be modelled as sensor noise and be accounted for in an augmented plant model described as follows:

$$\begin{cases} \dot{x} \\ \dot{x}_w \end{cases} = \begin{bmatrix} A & 0 \\ 0 & A_w \end{bmatrix} \begin{bmatrix} x \\ x_w \end{bmatrix} + \begin{bmatrix} B & B_{w1} \\ 0 & B_{w2} \end{bmatrix} \begin{bmatrix} u \\ w \end{bmatrix}, \\ \begin{bmatrix} z \\ y \end{bmatrix} = \begin{bmatrix} C_1 & 0 \\ C_2 & C_w \end{bmatrix} \begin{bmatrix} x \\ x_w \end{bmatrix} + \begin{bmatrix} 0 & 0 \\ D & 1 \end{bmatrix} \begin{bmatrix} u \\ v \end{bmatrix}, \quad (5)$$

where  $x \in \mathbb{R}^6$  represents the state of the three vibration modes to be controlled (M1, M2, M3) with state space

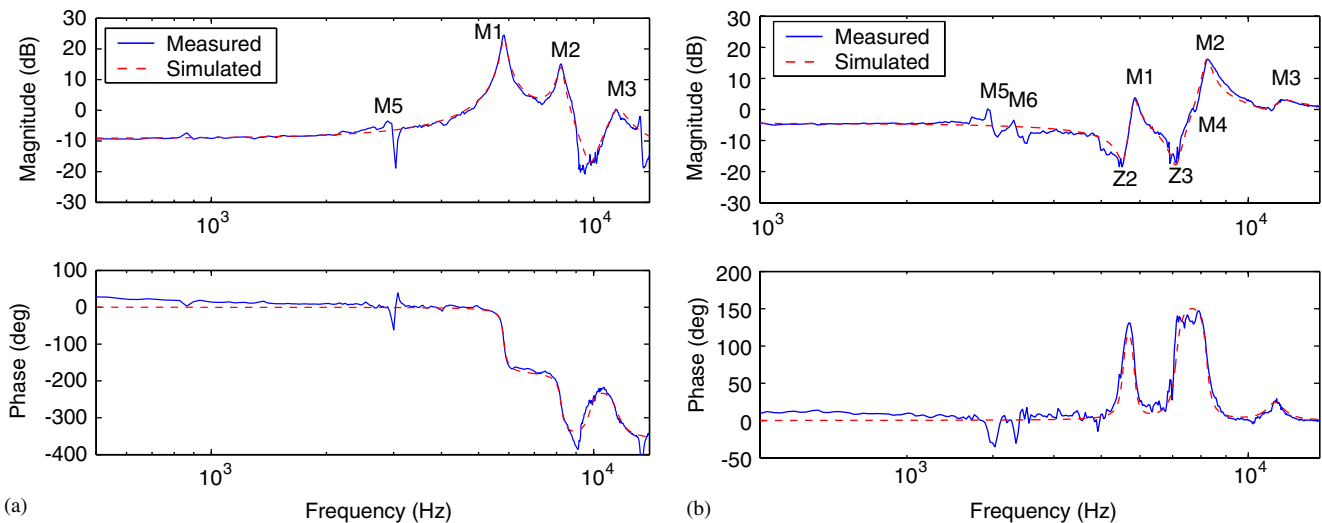


Fig. 9. PZT-actuated suspension frequency response: (a) from VCM input  $u_{VCM}$  to PZT sensor output  $y$ ; (b) from PZT actuator input  $u_{MA}$  to PZT sensor output  $y$ .



modal representation given by  $A, B, C_1, C_2$  and  $D$ ;  $x_w \in \mathbb{R}^6$  represents the state variables of the three noise modes (M5, M6, M7);  $u = [u_{VCM} \ u_{MA}]$  is the control input,  $w \in \mathbb{R}^6$  is a fictitious white disturbance vector used to characterize the excitation to each vibration mode by airflow disturbances;  $A_w$  is estimated from the measured PSD in Fig. 8;  $B_{w1}, B_{w2}$  and  $C_w$  are normalized. A discrete-time model of  $P$  in Eq. (5) is then derived, taking into account the computational-time delay  $t_d$ , which although smaller than the sampling time  $T_s$ , is significant and must be accounted for in the damping controller design (Li, 2003; Li, Marcassa, et al., 2003).

A discrete-time Kalman filter with prediction and correction steps was designed based on the augmented plant model. The state feedback damping controller gain  $K$  was determined by solving a linear quadratic regulator

(LQR) which minimizes

$$E\{z^2 + u_D^T R u_D\}, \tag{6}$$

where  $z$  is the head displacement output and  $u_D$  is the damping controller output. The design parameter in the LQR design is the positive definite control action weight matrix  $R$ , which can be tuned to obtain desired system responses.

The sampling frequency used for the inner-loop damping controller in Fig. 10 is 50 kHz, while that for the track-following controller is 25 kHz. The inner-loop vibration damping controller is designed first. Then, the outer-loop track-following controller is designed based on the damped actuator model, using the sensitivity decoupling design methodology discuss in Section 3.2. The gain crossover frequency, gain margin and phase margin of the open-loop transfer function of the control system were 2425 Hz, 3.4 dB, and 37°, respectively. A design similar to the one presented in Section 3.2.1 is used, except that no notch filters were required. Moreover, the bandwidth of the track-following controller with inner-loop damping control is larger than the one that used notch filters.

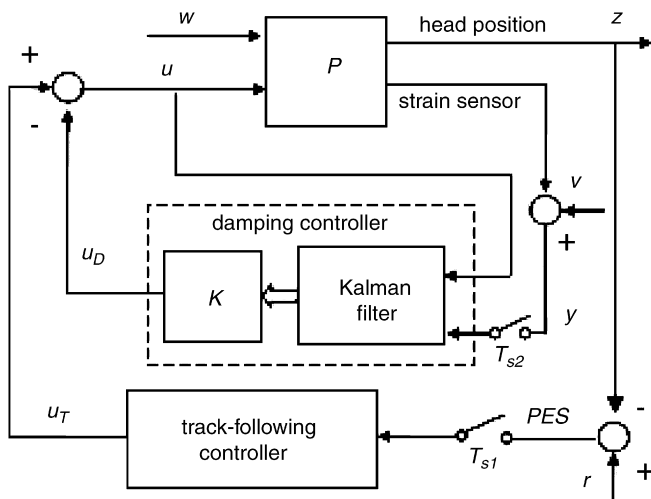


Fig. 10. Block diagram of a dual-stage servo system with inner-loop vibration damping control.

4.1.1. Experimental results

Figs. 11(a) and (b) compare the frequency responses of the damped system to those of the open-loop system, from the VCM and PZT actuator to the head displacement, respectively. Both the butterfly mode and the suspension sway mode are attenuated by damping control.

Fig. 12(a) shows the PSD of the head lateral motion measured by the LDV and the HP digital analyzer when damping control is and is not applied. As shown in the figure, the air turbulence excited high-frequency structural vibrations are attenuated by damping control. The RMS value of the PSD from 2 kHz to 14 kHz is reduced by 35% when damping control is applied. Fig. 12(b) shows the FFT of the head-off track motion under dual-stage

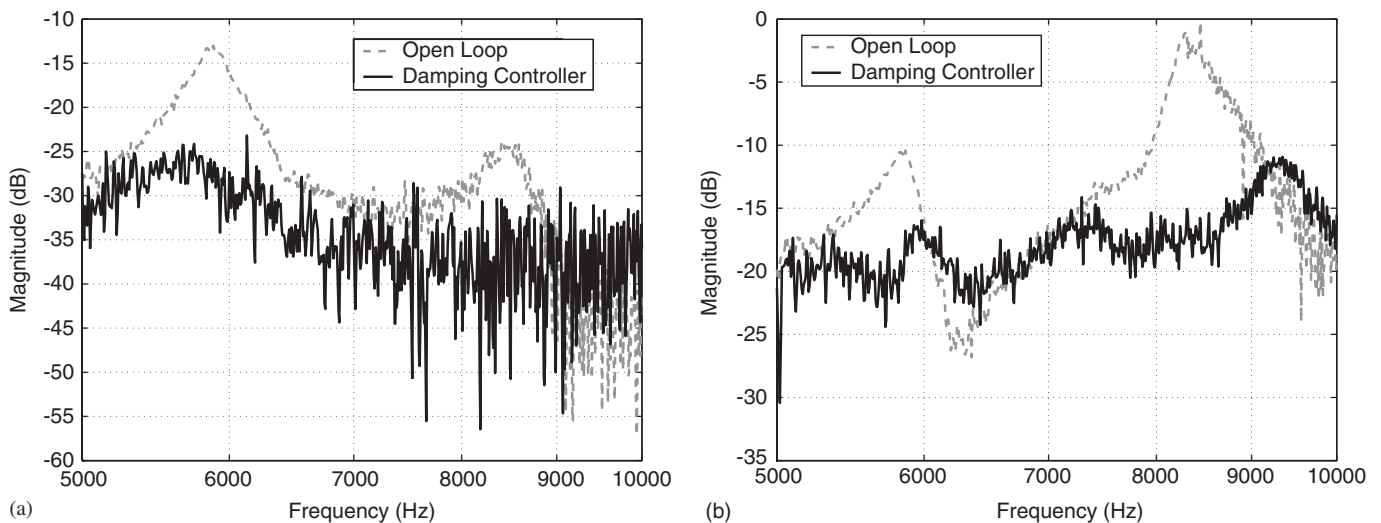


Fig. 11. Measured frequency response of a PZT-actuated suspension with and without active damping control: (a) from the VCM to the head displacement; (b) from the PZT actuator input to the head displacement.

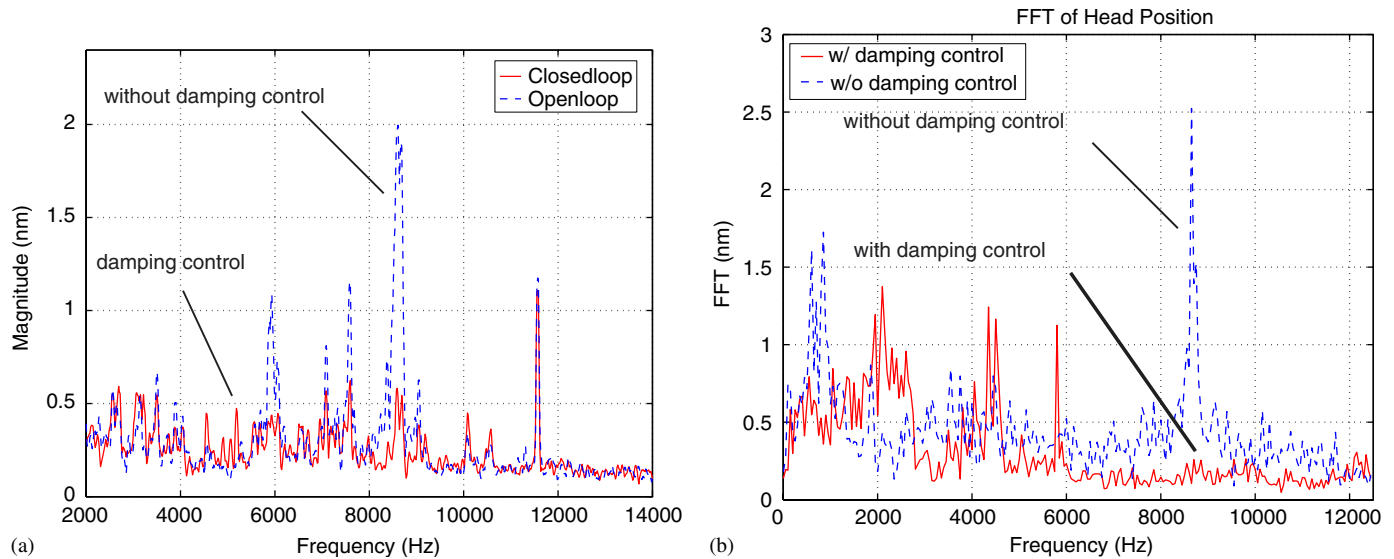


Fig. 12. (a) Measured PSD of head off-track motion with and without damping control; (b) FFT of the head off-track motion under track-following control with and without damping control.

track-following control. The solid line is the result with combined track-following and vibration damping control, while the dashed line is the result of using the track-following controller discussed in Section 3.2.1 without active damping control. High-frequency vibrations are greatly attenuated by the inner-loop vibration damping controller. The track-following controller with damping control also exhibits a larger disturbance attenuation in the low-frequency range because of its increased bandwidth. The standard deviation of the PES of the damping control design is 4.8 nm, while that of the traditional notch filter design is 6.1 nm.

## 5. Optimal strain sensor placement and fabrication in instrumented suspensions

As discussed in the previous section, instrumenting a disk drive suspension with vibration sensing strain gages can enhance vibration suppression in HDDs, provided that the gages are properly located and are sufficiently sensitive.

Many researchers have considered the problem of optimal placement of sensors on a flexible structure. Most often, sensors are placed according to some measure derived from system observability. Hac & Liu (1993) proposed a measure based on eigenvalues of the observability Grammian, which was later applied to disk drives (Banther, Huang, & Messner, 1998; Huang et al., 1999), while (Lim, 1996) proposed to use Hankel singular values to evaluate observability. Unfortunately, open-loop observability approaches do not necessarily provide an optimal location from a controlled, closed-loop perspective. These methods tend to concentrate optimization effort on hard-to-observe modes, regardless of their relative importance in contributing to a specific output. To remedy this shortcoming, some researchers have proposed using closed-loop

objectives instead, such as LQG (Kondoh, Yatomi, & Inoue, 1990). These approaches give a better indication of closed-loop optimality, but are typically heavily computationally intensive and their solutions generally do not provide any significant insight regarding the physical basis behind the choice of sensor location. Also of interest is the rejection of signals from unwanted modes; Wu, Rice, & Juang (1979) proposed a method for eliminating unwanted modes from the sensor output, while Gregozy (1984) has suggested methods for reducing the order of flexible systems. Recently, (Oldham, Kon, & Horowitz, 2003, 2004) has formulated a computationally simple method of evaluating the performance of a linear quadratic gaussian (LQG) controller for many possible sensor locations. In this section the results of (Oldham et al., 2003, 2004) are briefly reviewed.

The servo system described here consists of the flexible suspension with inputs from the VCM and airflow disturbances, plus an actuated-slider MA at the tip of the suspension, as depicted in Fig. 13(a). It should be noted that the suspension depicted in Fig. 13(a) is not a PZT-actuated suspension, such as the one described in Sections 3 and 4.1. This suspension was designed to carry a MEMS MA in between the slider and the gimbal, as described in Section 2.2.

The general optimal sensor placement problem can be formulated as described in the block diagram shown in Fig. 13(b). The plant itself, described by the transfer function  $G(s)$  in Fig. 13b, is a modal model of the suspension/MA/head assembly, with control inputs  $u$ , disturbance inputs  $w$ , and two outputs. The first output is the head position  $z$ . Notice that  $z$  has a fixed state model output matrix  $C_z$ , which is independent of the location and orientation of the vibration sensors. The multiple vibration sensor outputs are denoted by  $y$ . The state output matrix

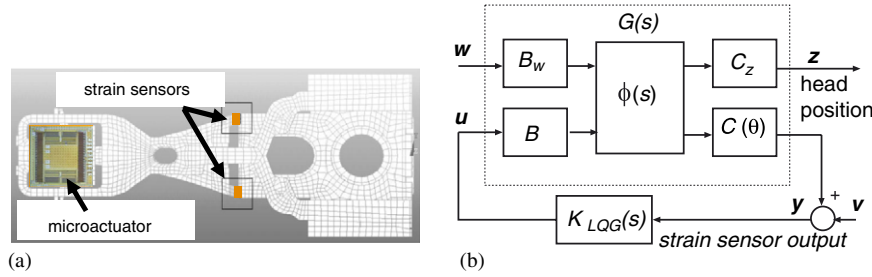


Fig. 13. (a) An Ansys model of a commercial MEMS-actuator ready suspension. Figures of an actuated-slider and strain sensors have been superimposed on the Ansys model; (b) block diagram for setting up the optimal sensor placement problem.

for these outputs,  $C(\theta)$ , are dependent on sensor locations (position and orientation), which is parameterized by the vector  $\theta$ . The system may have multiple control inputs,  $u$ , and disturbances,  $w$ , which enter through separate input matrices, respectively, denoted by  $B$  and  $B_w$ . The Laplace transform of the transition matrix,  $\Phi(s)$ , of the system is in modal form, with  $n$  distinct vibration modes.  $K_{LQG}(s)$  in Fig. 13(b) is an infinite horizon LQG regulator

$$K_{LQG}(s) = -K(sI - A + BK + FC)^{-1}F, \quad (7)$$

with state feedback gain,  $K$ , and Kalman filter gain,  $F$ , that minimizes the weighted sum of the system output  $z$  (the read/write head position) and control effort variances

$$J_{H2} = \min_{K,F} E\{z^2 + u^T R u\}. \quad (8)$$

The gain matrices  $K$  and  $F$  are obtained by solving the algebraic Riccati equations

$$\begin{aligned} A^T P + PA - PBR^{-1}B^T P + C_z^T C_z &= 0, \\ K &= R^{-1}B^T P, \end{aligned} \quad (9)$$

$$\begin{aligned} AM + MA^T - MC(\theta)^T V^{-1}C(\theta)M + B_w W B_w^T &= 0, \\ F &= MC(\Phi)^T V^{-1}. \end{aligned} \quad (10)$$

Matrices  $B$ ,  $C_z$ ,  $B_w$ , and  $C(\theta)$  in Eqs. (9) and (10) are the same input and output matrices shown in Fig. 13(b). The scalars  $V = E\{v^2\}$  and  $W = E\{w^2\}$  in Eq. (10) are the variances of the white, zero-mean and uncorrelated Gaussian sensor noise  $v$  and system disturbance input  $w$ , respectively. Finally, matrix  $A$  is the state space form of the transition matrix  $\Phi(s)$  in Fig. 13(b), such that  $\Phi(s) = [sI - A]^{-1}$ .

In Oldham et al. (2003, 2004) algebraic approximations for the terms of the Kalman filter algebraic Riccati equation (10) that appear in the steady-state LQG objective function (8) have been derived, eliminating many of the drawbacks of this approach. These approximations capitalize on the sparse and repetitive structure of matrices used to describe vibrating systems in modal coordinates. A modal state space realization of the plant transfer function

$G(s)$  and its associated transition matrix  $\Phi(s)$  is

$$A = \begin{bmatrix} A_1 & 0 & \cdots & 0 \\ 0 & A_2 & \cdots & 0 \\ \vdots & & \ddots & \vdots \\ 0 & \cdots & 0 & A_n \end{bmatrix}, \quad B = \begin{bmatrix} B_1 \\ B_2 \\ \vdots \\ B_n \end{bmatrix}, \quad B_w = \begin{bmatrix} B_{w1} \\ B_{w2} \\ \vdots \\ B_{wn} \end{bmatrix}, \quad (11)$$

$$A_i = \begin{bmatrix} 0 & \omega_i \\ -\omega_i & -2\xi_i \omega_i \end{bmatrix}, \quad B_i = \begin{bmatrix} 0 & \cdots & 0 \\ b'_{i1} \omega_i & \cdots & b'_{il} \omega_i \end{bmatrix},$$

$$B_{wi} = \begin{bmatrix} 0 & \cdots & 0 \\ b_{i1} \omega_i & \cdots & b_{il} \omega_i \end{bmatrix},$$

$$C(\theta) = \begin{bmatrix} c_{11}(\theta_1) & 0 & c_{12}(\theta_1) & 0 & \cdots & c_{1n}(\theta_1) & 0 \\ \vdots & \vdots & \vdots & \vdots & & \vdots & \vdots \\ c_{r1}(\theta_r) & 0 & c_{r2}(\theta_r) & 0 & \cdots & c_{rn}(\theta_r) & 0 \end{bmatrix},$$

$$C_z = [c_{z1} \ 0 \ \cdots \ c_{zn} \ 0].$$

In Eqs. (11)  $\omega_i$  and  $\xi_i$  are, respectively, the natural frequency and damping ratio of vibration mode  $i$ ,  $b'_{ik}$  is the gain from input  $k$  to mode  $i$ ,  $b_{ik}$  is the gain from stochastic disturbance  $k$  to mode  $i$ , and  $c_{zi}$  is the output gain from mode  $i$  to the objective output  $z$ , which in this case is the off-track error at the tip of the suspension. The terms  $c_{ji}$  represent the output gain from mode  $i$  to sensor  $j$ , and depend on the choice of sensor location, parameterized by vector  $\theta_j$ , which is the portion of vector  $\theta$  specific to sensor  $j$ .

When modes are well-spaced in frequency, and the contribution of the sensor noise,  $v$ , to the sensor output is large relative to the contribution of the input random disturbance,  $w$ , for all input and sensor coefficients in the modal system, such that the following condition is satisfied:

$$|c_{ji}| \left( \sum_{k=1}^l |b_{ik}| \right) \frac{W}{V} \ll 1 \quad \text{for all } i, j, \quad (12)$$

accurate algebraic approximations for the LQG objective function in Eq. (8) can be found. For example, in the simplest case of an undamped system under cheap control,

with  $n$  modes,  $m$  disturbances, and  $r$  sensors, the approximation is given by

$$J_{H2} \approx \sum_{i=1}^n \frac{c_{zi}^2 (\sum_{k=1}^m b_{ik}^2) \omega_i wv}{\sqrt{\sum_{j=1}^r c_{ji}^2}}. \quad (13)$$

Similar results exist for damped systems and non-cheap control, and these can be found in Oldham et al. (2003). In addition, it is important to note that the state feedback control gain  $K$  and controller Riccati solution  $P$  in Eq. (9) do not depend on sensor location. This permits straightforward extensions of the algebraic results presented here for the case of non-cheap control (Oldham et al., 2003). Fig. 15(a) illustrates the satisfaction of condition (12).

Approximating the objective function in this manner has several advantages. Its main one being that the approximation greatly simplifies the computation of the objective function by reducing the problem of solving for  $n$  eigenvalues to a straightforward algebraic computation. In our tests, this reduced computation time by a factor of 20. This is especially important for a system with many modes and/or sensor location variables. The approximation allows the optimal solution to be found easily for varying system parameters where an exact solution would be highly impractical. Moreover, the approximate solution also provides insights into the physical trade-offs between parameters of the system, and reduces the amount of knowledge needed about the system beforehand. Notice that the relative significance of the parameters in the system model in the cost function is clearly visible, in Eq. (13), which can be useful for design and interpretation. The best sensor locations will have large strains (large  $c_{ki}$  coefficients), as one would expect. However, in a choosing between strain contributions from different modes when there is a trade-off, a more optimal location will emphasize the mode with a larger contribution to off-track error, as computed from the sum of input coefficients to that mode, the  $b_{ip}$ 's, and the modal displacement coefficient at the slider,  $c_{zi}$ .

A commercial, MEMS-actuator-ready suspension, was modelled in ANSYS for finite element analysis of vibration

modes. A modal analysis was performed to identify the natural frequencies of vibration, followed by a harmonic analysis near those frequencies to obtain the frequency response of the structure. The analysis provided transfer functions from VCM input to off-track displacement and to  $x$ -normal,  $y$ -normal, and  $xy$ -shear components of strain at any model element. Subsequently, these strain components were projected to a voltage output for an arbitrary strain gage orientation  $\theta$  using Mohr's equation and the estimated gage sensitivity. Fig. 13(a) shows the full ANSYS model of the suspension. The figure also shows a picture of an actuated slider MEMS electrostatic actuator. The LQG cost function was evaluated at 100 high-strain elements in the hinge region of the suspension at sensor orientations from  $0^\circ$  to  $18^\circ$  for both the exact solution for the Kalman filter Riccati equation and for the approximate solution discussed above.

Fig. 14(a) and (b) show the 20 best elements for strain gage installation using both evaluations. Both the exact solution and the approximation identify element 1346 as optimal, with the strain gage oriented at  $11^\circ$  for the exact solution and  $10^\circ$  for the approximation. Similar results were obtained for non-cheap control (Oldham et al., 2003, 2004).

Fig. 15(a) shows the frequency responses from disturbance input to strain sensor output, when the sensor is located at various FEM elements and at different orientations. The figure also illustrates the satisfaction of condition (12). Fig. 15(b) shows a comparison between the predicted dynamic responses from the disturbance input to the head position,  $z$  and from the disturbance input to the sensor output  $y$ , when the sensor is located at the optimal location and orientation. As shown in the figure, the best sensor location will have both a high level of strain and a large ratio of strain to off-track response at each mode. This results in a frequency response that approximately matches the importance of modes at the sensor to their importance to off-track error at the slider, i.e. the modes with the largest contribution to off-track error also produce the largest response in the sensor output. For this sensor location, the most difficult mode to

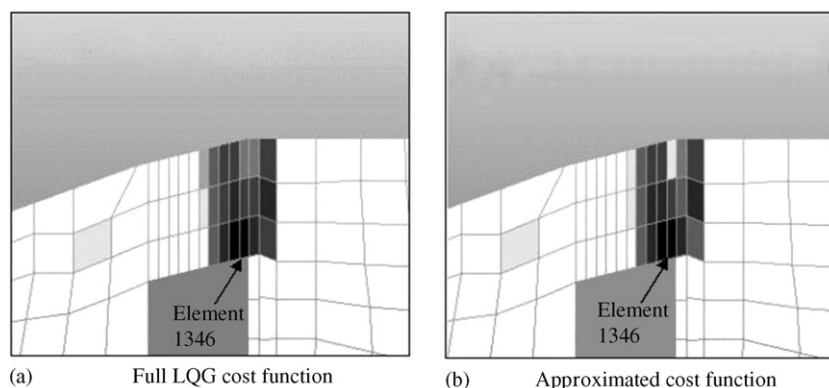


Fig. 14. (a) Exact and (b) approximated optimal sensor locations for LQG cheap control ( $R \rightarrow 0$ ).



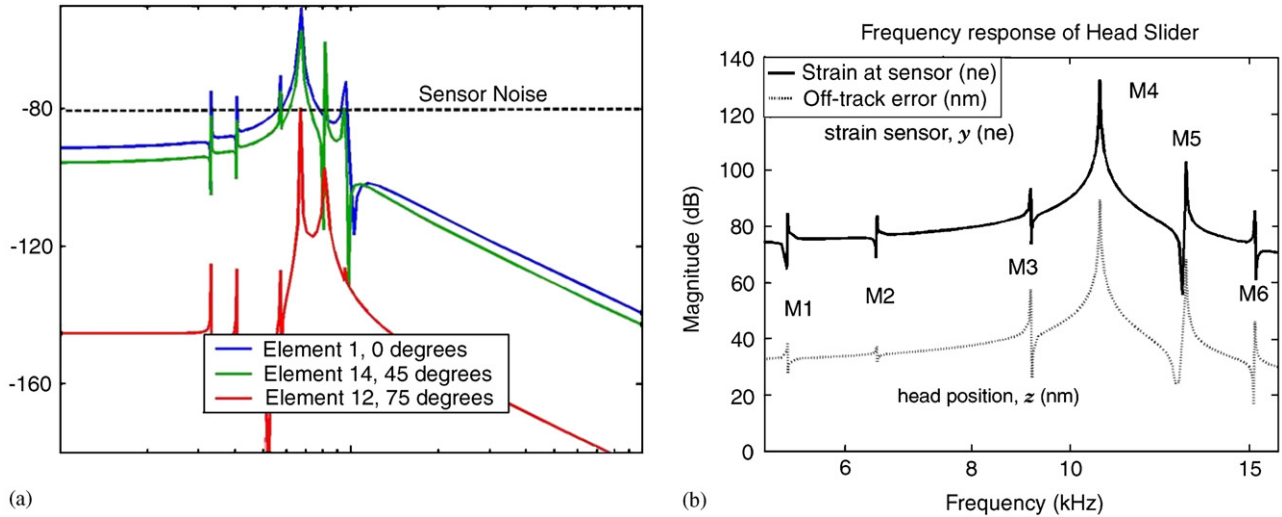


Fig. 15. (a) Strain frequency response at different FEM elements and sensor orientations and sensor noise level, indicating satisfaction of condition (12); (b) frequency responses of the head motion,  $z$  and strain sensor output  $y$  at its optimal location and orientation.

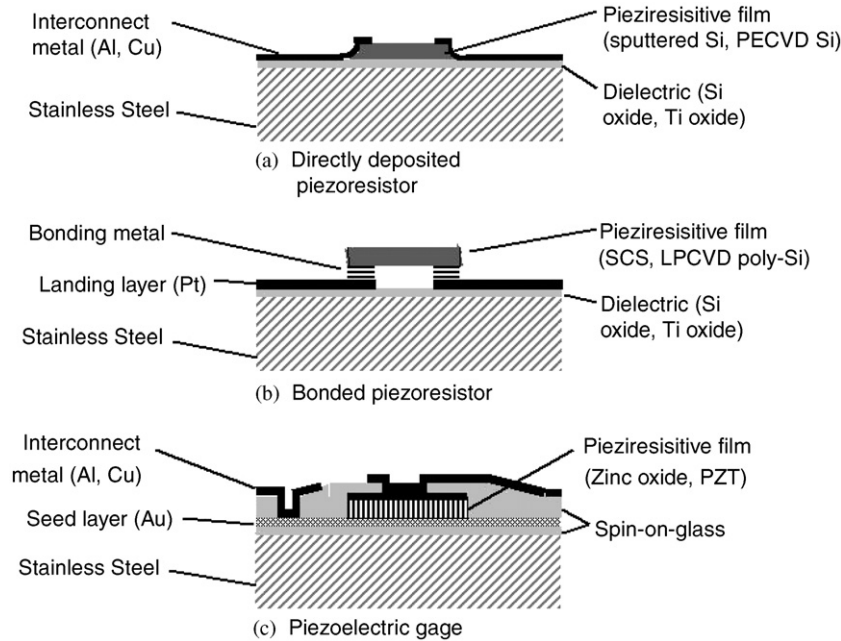


Fig. 16. Cross-sections of proposed strain sensors.

detect is mode M5 in Fig. 15(b), a torsion mode, for which a disturbance producing 1 nm off-track displacement would produce 56 nanostrain at the sensor location.

5.1. Isolation of specific vibration modes

Another advantage of using dedicated vibration sensors is the ability to isolate specific vibration modes, using superposition of multiple strain gage outputs. This approach may overcome problems such as those encountered in Section 4.1, where a PZT element, originally designed to be an actuator, was used as a sensor and detected vibration modes that contribute little to off-track error, such as modes M5, M6 and M7 in Fig. 8, which are

out-of-the-plane suspension bending vibration modes. For example, subtracting the signals produced by two identical strain sensors located at opposite sides of the suspension, as shown in Fig. 13(a), may significantly decrease or eliminate the contribution of out-of-the-plane suspension bending modes, while preserving the contribution of sway and torsion off-track modes to the overall strain sensing output.

5.2. Sensor fabrication

Several methods for installing strain gages at the locations identified by our optimization procedure are currently being explored. The sensors' targeted resolution

is 56 nanostrain, corresponding to a maximum of 1 nm displacement from any individual mode based on our optimization results. MEMS-style processing and photolithography permit fabrication of very small sensors at precise locations. Furthermore, highly sensitive materials, such as piezoresistive semiconductors and piezoelectric films are available. However, using these techniques and materials with steel substrates imposes certain constraints on the fabrication procedure. Any treatments to the substrate itself must be performed at low temperatures to avoid altering the suspension's material properties, thus limiting materials available for direct deposition. The finished device must also be robust enough to survive additional suspension processing steps, especially bending of the hinge region to set the suspension pre-load.

A comparison of various piezoresistive materials based on their gage factor, noise, and resolution for a single FEA element-sized 100  $\mu\text{m}$  long by 20  $\mu\text{m}$  wide strain gage and a  $5 \text{ nV}/\sqrt{\text{Hz}}$  electronics noise level reveals that conventional metal strain gages, such as constantan, are not sensitive enough for the necessary resolution without extremely clean circuitry. Semiconductor films deposited at low temperatures, such as amorphous hydrogenated silicon ( $\alpha\text{Si:H}$ ) tend to be limited by intrinsic thermal noise due to poor conductivity, but, adapted to a steel substrate, may still achieve the necessary resolution. A sensor of this type is shown in Fig. 16(a). Finally, single-crystal silicon and high-temperature polysilicon project the best performance, but these cannot be deposited directly on steel without violating temperature constraints.

To capitalize on the extreme sensitivity of single crystal silicon, piezoresistive sensors for bonding to a steel substrate are being constructed using a direct metal-on-metal bonding procedure developed by Microassembly Technologies, Inc. The proposed procedure is to pattern sensors on a handle wafer from a semiconductor film over a sacrificial oxide layer. Metal bumps will be formed on bonding points on the sensors. Meanwhile, an insulating film is deposited on the steel substrate, followed by a metal landing layer. This landing layer can be patterned to form leads to external bond pads. The two substrates are then pressed together, forming a metal-to-metal eutectic bond. The sensor is detached from the substrate either through fracture of thin tethers or of silicon oxide anchors. A sensor of this type is shown in Fig. 16(b). An alternative to piezoresistive sensing is to use a piezoelectric film, which may provide an even higher sensitivity than semiconductor materials. The difficulty of this approach is forming a high-quality piezoelectric film on a rough steel surface. Sputtered zinc oxide films with sensitivity as good as one-fifth that of bulk zinc oxide by planarizing the steel surface with spin-on-glass and using a gold seed layer was able to be deposited. This sensitivity projects to single nanostrain level sensor resolution, but the full processing sequence is yet to be tested. The zinc oxide film must be capped with an etch stopping layer, patterned into sensors, and topped with interconnects to external bond pads. A sensor of this

type is shown in Fig. 16(c). The performance of patterned zinc oxide sensors are currently being tested.

## 6. Conclusion

This paper discussed the use of dual-stage servo systems and instrumented suspensions in magnetic HDDs. In order to make the exposition coherent, the paper focused on the design and experimental implementation of dual-stage track-following servo systems and active damping feedback controllers using PZT-actuated suspensions and examined the design and fabrication of instrumented disk drive suspensions, focusing on the optimization of the strain sensor location and the development of MEMS-based strain sensor fabrication techniques. Related topics not covered in this paper are the design and implementation slider-actuated dual-stage servo systems for track-following and air flow-induced suspension vibration suppression, as well as the robust design of dual-stage and vibration suppression control systems using  $\mu$ -synthesis and mixed  $H_2/H_\infty$  techniques. Interested readers are referred to the references contained in this paper.

## References

- Banther, M., Huang, Y., & Messner, W. (1998). Optimal strain gauge placement for an instrumented disk drive suspension. In *Proceedings of American control conference* (pp. 3023–3027).
- Chen, T.-L. (2001). *Design and fabrication of PZT-actuated silicon suspensions for hard disk drives*. Ph.D. dissertation, University of California, Berkeley, CA, USA.
- de Callafon, R. A., Nagamune, R., & Horowitz, R. (2006). Robust dynamic modeling and control of dual-stage actuators. *IEEE Transactions on Magnetics*, 42(2), 247–254.
- Ehrlich, R., & Curran, D. (1999). Major hdd tmr sources, and projected scaling with tpi. *IEEE Transactions on Magnetics*, 35, 885–891.
- Evans, R. B., Griesbach, J. S., & Messner, W. C. (1999). Piezoelectric microactuator for dual-stage control. *IEEE Transactions on Magnetics*, 35, 977–981.
- Fan, L.-S., Hirano, T., Hong, J., Webb, P. R., Juan, W. H., Lee, W. Y., et al. (1999). Electrostatic microactuator and design considerations for hdd application. *IEEE Transactions on Magnetics*, 35, 1000–1005.
- Gregozy, C. Z. (1984). Reduction of large flexible spacecraft models using internal balancing theory. *Journal of Guidance Control & Dynamics*, 7(6), 725–732.
- Gross, H. (2003). *Off-track vibrations of the read-write heads in hard disk drives*. Ph.D. Dissertation, University of California, Berkeley, CA, USA.
- Hac, A., & Liu, L. (1993). Sensor and actuator location in motion control of flexible structures. *Journal of Sound and Vibration*, 167(2), 239–261.
- Hernandez, D., Park, S.-S., Horowitz, R., & Packard, A. K. (1999). Dual-stage track-following servo design for hard disk drives. In *Proceedings of American automatic control conference* (pp. 4116–4121).
- Herrmann, G., & Guo, G. (2004). Hdd dual-stage servo-controller design using a mu-analysis tool. *Control Engineering Practice*, 12(3), 241–251.
- Horsley, D. (1998). *Microfabricated electrostatic actuators for magnetic disk drives*. Ph.D. Dissertation, University of California, Berkeley, CA, USA.
- Hu, X., Guo, W., Huang, T., & Chen, B. M. (1999). Discrete time LQG/LTR dual-stage controller design and implementation for high track density HDDs. In *Proceedings of American automatic control conference* (pp. 4111–4115).

- Huang, X., & Horowitz, R. (2005). Robust controller design of a dual-stage disk drive servo system with an instrumented suspension. *IEEE Transactions on Magnetics*, 41(8), 2406–2413.
- Huang, X., Horowitz, R., & Li, Y. (2005). Track-following control with active vibration damping and compensation of a dual-stage servo system. *Microsystem Technologies*, 11(12), 1276–1286.
- Huang, X., Nagamune, R., & Horowitz, R. (2006). A comparison of multirate robust track-following control synthesis techniques for dual-stage and multisensing servo systems in hard disk drives. *IEEE Transactions on Magnetics*, 42(7), 1896–1904.
- Huang, X., Nagamune, R., Horowitz, R., & Li, Y. (2004). Design and analysis of a dual-stage disk drive servo system using an instrumented suspension. In *Proceedings of the American control conference (ACC)*.
- Huang, Y., Banther, M., Mathur, P., & Messner, W. (1999). Design and analysis of a high bandwidth disk drive servo system using an instrumented suspension. *IEEE/ASME Transactions on Mechatronics*, 4, 196–206.
- Imamura, T., Katayama, M., Ikegawa, Y., Ohwe, T., Koishi, R., & Koshikawa, T. (1998). MemS-based integrated head/actuator/slider for hard disk drives. *IEEE/ASME Transactions on Mechatronics*, 3, 166–174.
- Jorgenson, F. (1995). *Complete handbook of magnetic recording*. New York: McGraw-Hill.
- Kim, B.-C., & Mote, C. D. (1999). *Suppressing turbulence induced vibration of the head suspension assembly in a hard disk drive*. In *CML Technical Report*, number 99-015, University of California, Berkeley, USA.
- Koganezawa, S., Takaishi, K., Mizoshita, Y., Uematsu, Y., & Yamada, T. (1997). Development of integrated piggyback milli-actuator for high density magnetic recording. In *International conference on micro-mechatronics for information and precision equipment* (pp. 20–23).
- Kondoh, S., Yatomi, C., & Inoue, K. (1990). The position of sensors and actuators in vibration control of flexible systems. *JSME International Journal, Series III*, 33, 145–152.
- Kuwajima, H., & Matsuoka, K. (2002). Thin film piezoelectric dual-stage actuator for hdd. In *InterMag Europe, Session BS04*.
- Li, Y. (2003). *Dual-stage servo control and active vibration compensation in magnetic hard disk drives*. Ph.D. Dissertation, University of California, Berkeley, CA, USA.
- Li, Y., & Horowitz, R. (2001). Mechatronics of electrostatic micro-actuators for computer disk drive dual-stage servo systems. *IEEE/ASME Transactions on Mechatronics*, 6(2), 111–121.
- Li, Y., & Horowitz, R. (2002). Design and testing of track-following controllers for dual-stage servo systems with pzt actuated suspensions. *Microsystem Technologies*, 8, 194–205.
- Li, Y., Horowitz, R., & Evans, R. (2003). Vibration control of a pzt actuated suspension dual-stage servo system using a pzt sensor. *IEEE Transactions on Magnetics*, 39(2), 932–937.
- Li, Y., Marcassa, F., Horowitz, R., Oboe, R., & Evans, R. (2003). Track-following control with active vibration damping of a pzt-actuated suspension dual-stage servo system. In *Proceedings of American control conference* (Vol. 3).
- Lim, K. B. (1996). Disturbance rejection approach to actuator and sensor placement. *Journal of Guidance*, 20(1), 202–204.
- Mori, K., Munemoto, T., Otsuki, H., Yamaguchi, Y., & Akagi, K. (1991). A dual-stage magnetic disk drive actuator using a piezoelectric device for a high track density. *IEEE Transactions on Magnetics*, 27, 5298–5300.
- Muller, L. (2000). *Gimballed electrostatic microactuators with embedded interconnects*. Ph.D. Dissertation, University of California, Berkeley, CA, USA.
- Nagamune, R., Huang, X., & Horowitz, R. (2005). Multi-rate track-following control with robust stability for a dual-stage multi-sensing servo system in HDDs. In *Proceedings of the joint 44th IEEE conference on decision and control (CCDC) and European control conference (ECC)*.
- Naniwa, I., Nakamura, S., Saegusa, S., & Sato, K. (1999). Low voltage driven piggy-back actuator of hard disk drives. In *IEEE international MEMS 99 conference* (pp. 49–52).
- Oldham, K., Kon, S., & Horowitz, R. (2003). *Fabrication and optimal strain sensor placement in an instrumented disk drive suspension for vibration suppression*. CML Blue Report.
- Oldham, K., Kon, S., & Horowitz, R. (2004). Fabrication and optimal strain sensor placement in an instrumented disk drive suspension for vibration suppression. In *Proceedings of the 2004 American control conference* (pp. 1855–1861.) Boston, Massachusetts, June 30–July 2, 2004.
- Rotunno, M., & de Callafon, R. A. (2000). Fixed order  $H_\infty$  control design for dual-stage hard disk drives. In *Proceedings of the 39th IEEE conference on decision and control* (pp. 3118–3119).
- Schroeck, S. J., Messner, W. C., & McNab, R. J. (2001). On compensator design for linear time-invariant dual-input single-output systems. *IEEE/ASME Transactions on Mechatronics*, 6, 50–57.
- Semba, T., Hirano, T., & Fan, L.-S. (1999). Dual-stage servo controller for hdd using mems actuator. *IEEE Transactions on Magnetics*, 35, 2271–2273.
- Suh, S.-M., Chung, C. C., & Lee, S.-H. (2002). Design and analysis of dual-stage servo system for high track density hdds. *Microsystem Technologies*, 8, 161–168.
- Suthasan, T., Mareels, I., & Al-Mamun, A. (2004). System identification and controller design for dual actuated hard disk drive. *Control Engineering Practice*, 12(6), 665–676.
- Suzuki, T., Usui, T., Sasaki, M., Fujisawa, F., Yoshida, T., & Hirai, H. (1997). Comparison of robust track-following control systems for a dual stage hard disk drive. In *Proceedings of international conference on micromechatronics for information and precision equipment* (pp. 101–118).
- Wu, Y. W., Rice, R. B., & Juang, J. N. (1979). Sensor and actuator placement for large flexible space structures. In *Journal of automatic controls conference* (pp. 230–236).
- Yamaguchi, T. (2001). Modelling and control of a disk file head-positioning system. *Proceedings of the Institution of Mechanical Engineers, Part I (Journal of Systems and Control Engineering)*, 215, 549–567.
- Yamaguchi, Y., Takahashi, K., Fujita, H., & Kuwahara, K. (1986). Flow induced vibration of magnetic head suspension in hard disk drive. *IEEE Transactions on Magnetics*, 22(5), 1022–1024.